Available online at www.eccomasproceedia.org
Eccomas Proceedia COMPDYN (2021) 354-366

ECCOMAS
Proceedia

COMPDYN 2021
8th ECCOMAS Thematic Conference on
Computational Methods in Structural Dynamics and Earthquake Engineering
M. Papadrakakis, M. Fragiadakis (eds.)
Streamed from Athens, Greece, 28 - 30 June 2021

MICROMECHANICAL ANALYSIS OF UNREINFORCED AND REINFORCED MASONRY ARCHES

Daniela Addessi, Cristina Gatta, Mariacarla Nocera and Domenico Liberatore

Department of Structural and Geotechnical Engineering, Sapienza University of Rome
Via Eudossiana 18, 00184 Rome, Italy
e-mail: {daniela.addessi,cristina.gatta,mariacarla.nocera,domenico.liberatore}@uniroma1.it

Abstract. *This work analyzes the in-plane response of unreinforced and reinforced masonry arches by adopting micromechanical finite element (FE) models. These allow to describe onset and evolution of degrading mechanisms until failure, including the accurate characterization of the pre- and post-peak behavior. Two different models are adopted: the first considers each masonry component, brick and mortar, as continuous material discretized with quadrilateral FEs; the second connects properly resized bricks through interfaces representing both mortar and mortar-units interaction. Linear elastic behavior is assumed for bricks, whereas a coupled damage-friction constitutive law is adopted for mortar to account for typical arch collapse mechanisms involving flexural hinges and shear sliding. As concerns the modeling of the reinforcements, these are considered as truss elements with bilinear response in tension. In such a way the debonding and delamination phenomena are accounted in a simplified way.*

Results obtained with the proposed models are validated through comparison with experimental data and solutions obtained from other numerical approaches. It emerges that the response of both the unreinforced and reinforced elements are satisfactorily described, as well as the positive effect of the introduction of the reinforcement on the collapse load and failure mechanism.

Keywords: Micromechanical modeling, Finite element, Masonry arch, Reinforcement.

ISSN:2623-3347
Peer-review under responsibility of the organizing committee of COMPDYN 2021.
doi:10.7712/120121.8489.19128

1 INTRODUCTION

Most of historical masonry constructions, including monuments, urban buildings and bridges, are based on arch systems. These typically show high carrying capacity under gravity loads, but under point loads or seismic actions the thrust line falls outside the arch central core, inducing tensile stresses with the onset and growth of microcracks which, eventually, lead to the structural collapse. A traditional strengthening technique consists of the insertion of tie-rods which, however, have a strong visual impact and in some cases are not accepted. The scientific community proposed and developed several types of alternative strengthening techniques aimed at improving the arch performance with no visual impact and with negligible added mass. These are based on innovative composite materials consisting of glass fibers, carbon fibers, steel rod or other materials embedded in polymer or mortar matrices. Several experimental campaigns proved the efficiency of such strengthening systems [1], which usually increase the structural capacity in terms of both ductility and maximum strength. Apparently, the type of reinforcement and matrix [2, 3] and the reinforcement location [4, 5] significantly affect the overall response. Moreover, the classical collapse mechanism of unreinforced arches, involving the formation of four flexural hinges, is modified for strengthened structures. The failure modes are, in fact, usually characterized by shear sliding, masonry crushing, reinforcement rupture, debonding and delamination phenomena [1].

The experimental research is developed together with the formulation of efficient numerical models to reproduce and predict the arch structural response. In this framework, limit analysis approach is a consolidated tool for the assessment of the arch safety. Starting from the first applications of Heyman [6], many other enriched models have been proposed, where Heyman's hypotheses are partially or all removed [7, 8, 9] . The success of these models is mainly due to their simplicity and the reduced number of material parameters required in the analysis. The main limit is that no information is given on the pre- and post-peak response as well as the evolution process of the nonlinear mechanisms. To overcome these restrictions, accurate nonlinear finite element (FE) models have been developed [10, 11, 12]. Most of these are typically based on micromechanical, multiscale and macromechanical approaches [13, 14] and introduce nonlinear constitutive laws to describe the onset and evolution of degrading mechanisms. In particular, detailed micromechanical finite element formulations model each masonry constituent, brick and mortar, and their interaction. However, some simplified hypotheses are usually assumed to reduce the computational complexity, still ensuring enough accurate results. Neglecting the explicit modeling of the unit-mortar interfaces, the composite masonry material is regarded as the assembly of bricks/units and mortar joints which simultaneously describe mortar material and interfaces. According to this approach, in this work two strategies are adopted and compared to analyze the in-plane response of masonry arches. The first model, recently presented in [15], considers masonry components, units and mortar, as continuous materials discretized with quadrilateral FEs. Conversely, in the second model, masonry is modeled as the assembly of expanded units and interface elements representing both mortar and unit-mortar interaction. The two models are based on the same constitutive hypotheses, i.e. linear elastic and nonlinear behavior are assumed for bricks and mortar, respectively. The damage-friction law originally proposed in [16] is employed for joints. This allows to capture the typical failure modes of arches due to fracture mode I and II, and has been recently extended to mortar joints modeled as 2D [17] or 3D [18] interfaces. Moreover, when dealing with strengthened arch systems, reinforcements are modeled with truss elements, whose constitutive response is properly identified to also reproduce the debonding and delamination phenomena in a simplified

and conventional way [8, 10, 19].

To prove the capability of the proposed models to reproduce the response of unreinforced and reinforced arches, some numerical applications are performed on properly selected experimental tests. The results, in terms of global response curves and failure mechanisms, are compared with the experimental outcomes, as well as with those obtained by means of different FE numerical approaches.

2 MICROMECHANICAL FINITE ELEMENT MODELS

Two micromechanical FE models are presented to investigate the response of masonry arches. Both adopt isoparametric quadrilater FEs to discretize the bricks, but differ in the way the mortar joints are modeled. The first (Figure 1(a)), named as *continuous model* (CM), also uses isoparametric quadrilater FEs to describe mortar as continuous materials. The second (Figure 1(b)), later called as *interface model* (IM), adopts interface elements to model the mortar joints. Moreover, truss elements are used to introduce in a simple but effective way the strengthening material.

In the following, details about the constitutive assumptions made for brick, mortar and reinforcement are provided. Figure 2 gives a summary of the modeling choices.

Figure 1: Micromechanical models: masonry as the assembly of (a) bricks and mortar joints, (b) interfaces and expanded bricks.

2.1 Constitutive laws of masonry constituent materials and reinforcement

Similar constitutive hypotheses hold for the two micromechanical models CM and IM, as both assume nonlinear mechanisms only occurring in the mortar and linear-elastic response for units. Plane stress conditions are considered. Hence, the linear elastic relation between stresses, $\boldsymbol{\sigma}^b = \left\{\sigma_1^b \, \sigma_2^b \, \tau_{12}^b\right\}^T$, and strains $\boldsymbol{\varepsilon}^b = \left\{\varepsilon_1^b \, \varepsilon_2^b \, \gamma_{12}^b\right\}^T$, holds for bricks:

$$\boldsymbol{\sigma}^b = \mathbf{C}^b \boldsymbol{\varepsilon}^b \tag{1}$$

being $\mathbf{C}^b$ the elastic constitutive matrix for 2D plane stress problems, depending on the Young's modulus E^b and Poisson coefficient ν^b.

As for the mortar, the damage-friction law proposed in [16, 17] is assumed. This is properly formulated to analyze the response of arbitrarily curved masonry elements with variable inclination of mortar joints [15]. The constitutive law accounts for the typical flexural and shear degrading mechanisms characterizing masonry nonlinear behavior, that is degradation due to the onset of microcracks, friction effects caused by closure of microcracks in compression and unilateral stiffness recovery.

Herein, the main governing equations are recalled, specializing them on the basis of the modeling approach, CM or IM, adopted for the mortar. Indeed, stresses, $\boldsymbol{\sigma}$, and strains, $\boldsymbol{\varepsilon}$, are the static and kinematic descriptors of the mortar as continuous material, whereas tractions,

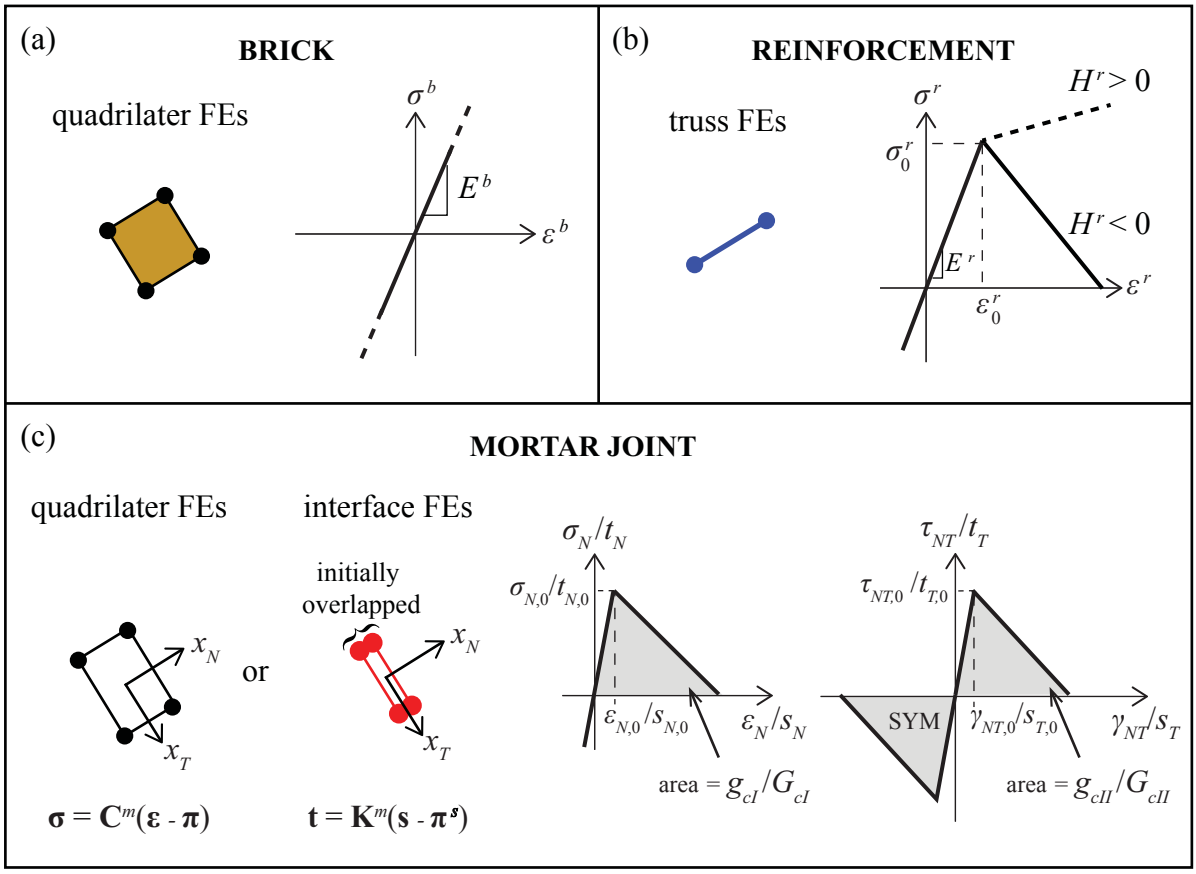

Figure 2: Types of finite elements and constitutive laws adopted for: (a) brick, (b) reinforcement and (c) mortar.

$\mathbf{t}$, and displacement jumps, $\mathbf{s}$, are the corresponding quantities in case of interfaces modeling mortar joints.

The constitutive law is firstly defined in the local reference system (x_T, x_N) of each mortar layer, being T and N the directions aligned with mortar joint width and thickness (Figure 1(c)). Then, it is expressed in the global system (x_1, x_2) by using standard transformation rules. The constitutive law for the CM is expressed as:

$$\underbrace{\begin{bmatrix}\sigma_T\\ \sigma_N\\ \tau_{NT}\end{bmatrix}}_{\boldsymbol{\sigma}} = \mathbf{C}^m\left(\underbrace{\begin{bmatrix}\varepsilon_T\\ \varepsilon_N\\ \gamma_{NT}\end{bmatrix}}_{\boldsymbol{\varepsilon}} - D\underbrace{\begin{bmatrix}h(\varepsilon_N)\varepsilon_T\\ h(\varepsilon_N)\varepsilon_N\\ \gamma_{NT}^p\end{bmatrix}}_{\boldsymbol{\pi}}\right) \tag{2}$$

where $\mathbf{C}^m$ is the mortar elastic constitutive matrix for plane stress conditions and $\boldsymbol{\pi}$ is the inelastic strain vector accounting for damage D, unilateral contact and slip γ_{NT}^p.

Similarly, tractions $\mathbf{t}$ at the interfaces are computed as:

$$\underbrace{\begin{bmatrix}t_T\\ t_N\end{bmatrix}}_{\mathbf{t}} = \mathbf{K}^m\left(\underbrace{\begin{bmatrix}s_T\\ s_N\end{bmatrix}}_{\mathbf{s}} - D\underbrace{\begin{bmatrix}s_T^p\\ h(s_N)s_N\end{bmatrix}}_{\boldsymbol{\pi}^s}\right) \tag{3}$$

being $\mathbf{K}^m$ the diagonal matrix collecting the stiffness values, K_T and K_N, along the tangential and normal directions, respectively, to the interface. In Eqs. (2) and (3), $h(\bullet)$ denotes the Heaviside function ($h(\bullet) = 1$, if $\bullet \geq 0$ and $h(\bullet) = 0$ otherwise), describing the unilateral stiffness

recovery due to the re-closure of the tensile cracks in compression.
According to its physical meaning, the damage variable D can range between 0 and 1, representing virgin and fully degraded material states, respectively. Its evolution law is stated as:

$$D = \max_{history} \left\{ 0 \, , \min \left\{ 1, \frac{1}{\eta} \left(\frac{\beta}{1+\beta} \right) \right\} \right\} \tag{4}$$

where β is the damage associated variable which assumes the following forms for continuous and interface mortar, respectively:

$$\beta = \sqrt{\left(\frac{\langle \varepsilon_N \rangle_+}{\varepsilon_{N,0}} \right)^2 + \left(\frac{\gamma_{NT}}{\gamma_{NT,0}} \right)^2} - 1, \qquad \beta = \sqrt{\left(\frac{\langle s_N \rangle_+}{s_{N,0}} \right)^2 + \left(\frac{s_T}{s_{T,0}} \right)^2} - 1 \tag{5}$$

In Eq. (5), the Macaulay's brackets $\langle \bullet \rangle_+$ select the positive part of the quantity; $\varepsilon_{N,0}$ and $\gamma_{NT,0}$ are the first crack strains, while $s_{N,0}$ and $s_{T,0}$ are the displacement jumps at the onset of the damaging mechanism (see Figure 2(c)).
Parameter η introduced in Eq. (4) rules the coupling of mode I and II of fracture, and assumes the following expression for CM:

$$\eta = 1 - \frac{1}{\alpha^2} \left[\langle \varepsilon_N \rangle_+^2 \, \eta_N + (\gamma_{NT})^2 \eta_{NT} \right] \qquad \text{with} \quad \alpha = \sqrt{\langle \varepsilon_N \rangle_+^2 + (\gamma_{NT})^2} \tag{6}$$

being η_T and η_{NT} quantities defined on the basis of the peak values of the stresses, $\sigma_{N,0}$ and $\tau_{NT,0}$, and the mode I and II fracture energy densities, g_{cI} and g_{cII}, as:

$$\eta_N = \frac{\sigma_{N,0} \, \varepsilon_{N,0}}{2 \, g_{cI}} \, , \qquad \eta_{NT} = \frac{\tau_{NT,0} \, \gamma_{NT,0}}{2 \, g_{cII}} \tag{7}$$

As for IM, the expressions corresponding to Eqs. (6) and (7) are obtained simply introducing the peak tractions, $t_{N,0}$ and $t_{T,0}$, the displacement jumps, $s_{N,0}$ and $s_{T,0}$, and the fracture energies for unit area, G_{cI} and G_{cII}.

Finally, the classical Mohr-Coulomb yield function is adopted to govern the evolution of the inelastic slip, γ_{NT}^p , modeling the frictional mechanisms at the interface between mortar and bricks for CM:

$$\varphi(\boldsymbol{\sigma}^d) = \mu \, \sigma_N^d + |\tau_{NT}^d| \tag{8}$$

or s_T^p for IM,

$$\varphi(\mathbf{t}^d) = \mu \, t_N^d + |t_T^d| \tag{9}$$

being μ the friction parameter. Then, the following non-associated flow rules are considered:

$$\dot{\gamma}_{NT}^p = \dot{\lambda} \frac{\tau_{NT}^d}{|\tau_{NT}^d|} \, , \qquad \dot{s}_T^p = \dot{\lambda} \frac{t_T^d}{|t_T^d|} \tag{10}$$

together with the Kuhn-Tucker loading-unloading conditions. The resulting constitutive responses for mode I and mode II are schematically depicted in Figure 2(c).

As concerns the constitutive response in tension of the truss element modeling the reinforcement layer, the bilinear elastic-damage law proposed in [20] is adopted:

$$\sigma^r = (1 - D^r) \, E^r \, \varepsilon^r \tag{11}$$

where D^r is the damage variable evolving on the basis of the following rule:

$$D^r = \max_{history} \left\{ 0, \ \frac{|\varepsilon^r - \varepsilon_0^r|}{\varepsilon^r} \left(1 - \frac{H^r}{E^r} \right) \right\} \tag{12}$$

As emerges from Figure 2(b), the resulting stress-strain relationship in compression is linear elastic and in tension is bilinear, with the first elastic branch characterized by stiffness E^r and the second branch described by the reduced stiffness H^r. In case, the constitutive relationship in Eq. (11) and the damage evolution law in Eq. (12) could easily be modified and enriched to describe the typical trilinear responses of composite reinforcement under tensile loads [3, 21].

2.2 Regularization techniques

The constitutive relationships adopted for reinforcements and mortar joints exhibit strain softening branches, as clearly shown in Figure 2(b,c). This means that the typical pathological mesh-dependency would affect the numerical FE response, if no proper regularization techniques are applied in the case of the continuous models adopted for the mortar and the reinforcement. In this work, two different regularization strategies are assumed: the nonlocal integral approach and the fracture energy technique.

The evolution problem of damage in each mortar joint is ruled by nonlocal quantities. In particular, variables β, η and α in Eqs. $(5)_a$ and (6) are evaluated on the basis of the nonlocal strain vector $\bar{\boldsymbol{\varepsilon}}$. At the generic point $\mathbf{x}$ of the k-th mortar joint, $\bar{\boldsymbol{\varepsilon}}$ is defined as:

$$\bar{\boldsymbol{\varepsilon}}(\mathbf{x}) = \frac{1}{\int_{\Omega^k} \psi(\mathbf{x},\mathbf{y}) d\Omega^k(\mathbf{y})} \int_{\Omega^k} \psi(\mathbf{x},\mathbf{y}) \boldsymbol{\varepsilon}(\mathbf{y}) d\Omega^k(\mathbf{y}) \tag{13}$$

where Ω^k denotes the area of the mortar joint k. The weight function ψ, measuring the influence of the point placed at $\mathbf{y}$ on the analyzed point located at $\mathbf{x}$, is assumed as the classical Gaussian function. This latter depends on the nonlocal radius l_c related to the characteristic length of the mortar. No interaction between different joints is accounted for.

The fracture energy approach is employed to regularize the numerical response of the reinforcement. This is a consolidated tool based on the adjustment of the post-peak slope of the stress-strain law depending on the size of the element. To this end, the stress-strain curve is properly modified. The energy dissipated in the finite element is equal to G^r, i.e. the assigned value in tension. A characteristic length l^e is defined for each truss element. The specific fracture energy g^r, defined in Eq. (14), is then scaled so that it results $g^r l^e = G^r$ for each truss element with:

$$g^r = \int_{\varepsilon_0^r}^{\varepsilon^r} \sigma^r(\varepsilon^r) d\varepsilon^r + \frac{1}{2} \sigma_0^r \varepsilon_0^r \tag{14}$$

For each scaled g^r, the corresponding value of the reduced stiffness H^r is defined, with the aim of evaluating the evolution of damage, as described in Eq. (12).

3 CORRELATION STUDIES: EXPERIMENTAL-NUMERICAL COMPARISON

Capability of the presented models in describing mechanical response of arch systems is evaluated with reference to the experimental campaign performed by Oliveira et al. [5]. The

tests investigated the response of twelve segmental half-scaled masonry arches subjected to increasing concentrated load applied at the quarter span up to failure. Two unreinforced arches, called US1 and US2, were tested and their reference response was used to evaluate the efficiency of strengthening techniques. The remaining samples were strengthened with different arrangements of GFRP (Glass Fiber-Reinforced polymer) strips. Continuous and localized strips were located at the intrados and/or extrados, also varying the reinforcement width.
Each arch was built with clay bricks (size $100 \times 50 \times 25\,\mathrm{mm}^3$) assembled with $10\,\mathrm{mm}$ thick mortar joints. Figure 3(a) shows the resulting geometry characterized by an internal span and radius equal to $1467\,\mathrm{mm}$ and $750\,\mathrm{mm}$, respectively, thickness $50\,\mathrm{mm}$ and out-of-plane width $450\,\mathrm{mm}$.

In the following, the mechanical response of the arches is numerically reproduced and the results are compared with the experimental outcomes and those derived by other numerical approaches. Particular attention is devoted to the analysis of the onset and evolution of the degrading mechanisms and the variation of the maximum load and failure mode caused by the presence of the reinforcement.

3.1 Response of unreinforced arches

The response of the unreinforced arches US1 and US2 is analyzed adopting both CM and IM. The first model, CM, discretizes each brick and mortar joint with 5×3 and 5×1 quadrilateral isoparametric FEs, respectively. The last, IM, adopts a similar discretization for the resized units, but 5×1 zero-thickness interface elements for each joint. As for the mechanical parameters of the constituent materials, these are set according to the available experimental data [5] and the numerical analyses performed by Di Re et al. [11]. Tables 1 and 2 contain the mortar mechanical parameters assumed for CM and IM, respectively. In detail, Table 2 shows the same quantities of Table 1 but expressed for the interfaces, and derived assuming that each interface models a mortar joint with a constant thickness equal to $l^m = 10\,\mathrm{mm}$. Consequently, $K_N = E^m/l^m$, $K_T = G^m/l^m$, $G_{cI} = g_{cI} \times l^m$ and $G_{cII} = g_{cII} \times l^m$ are set. Young's modulus $E^b = 5000\,\mathrm{MPa}$ and Poisson ratio $\nu^b = 0.2$ are assumed for bricks when adopting the continuous model. Instead, a scaled value $E^{b^*} = 7000\,\mathrm{MPa}$ is considered for IM to account for brick scaling and, consequently, describe the correct initial stiffness of the arches. Considering that resized bricks have length $l = l^b + l^m$, E^{b^*} is evaluated as $E^{b^*} = \frac{l}{l^b} E^b$.

E^m [MPa]	G^m [MPa]	$\sigma_{N,0}$ [MPa]	$\tau_{NT,0}$ [MPa]	g_{cI} [MPa]	g_{cII} [MPa]	μ
1200	500	0.25	0.25	1.8×10^{-3}	1.25×10^{-3}	0.5774

Table 1: Mechanical properties adopted for the mortar (CM).

K_N [N/mm^3]	K_T [N/mm^3]	$t_{N,0}$ [MPa]	$t_{T,0}$ [MPa]	G_{cI} [N/mm]	G_{cII} [N/mm]	μ
120	50	0.25	0.25	1.8×10^{-2}	1.25×10^{-2}	0.5774

Table 2: Mechanical properties adopted for the mortar joint interfaces (IM).

The numerical simulations are performed assuming for both materials unit weight $\gamma = 17\,\mathrm{kN/m}^3$ and imposing a concentrated monotonically increasing load under displacement control at the nineteenth brick counted from the left impost, mimicking the loading conditions in

Figure 3(a). The global response of the arch is depicted in Figure 3(b) in terms of vertical force F-vertical displacement s. The dashed blue lines correspond to the experimental outcomes, the green curve is that evaluated with the IM and the red line refers to the numerical results derived from the CM, and already presented in [15], assuming the nonlocal radius equal to the mortar characteristic length, that is $l_c = 10\,\mathrm{mm}$. Finally, for further comparison, the black curve shows the results of the multiscale model proposed by Di Re et al. [11], which adopts the same constitutive modeling assumptions but employs a force-based beam formulation in conjunction with the energy regularization technique. On the overall, a very good agreement is detected between

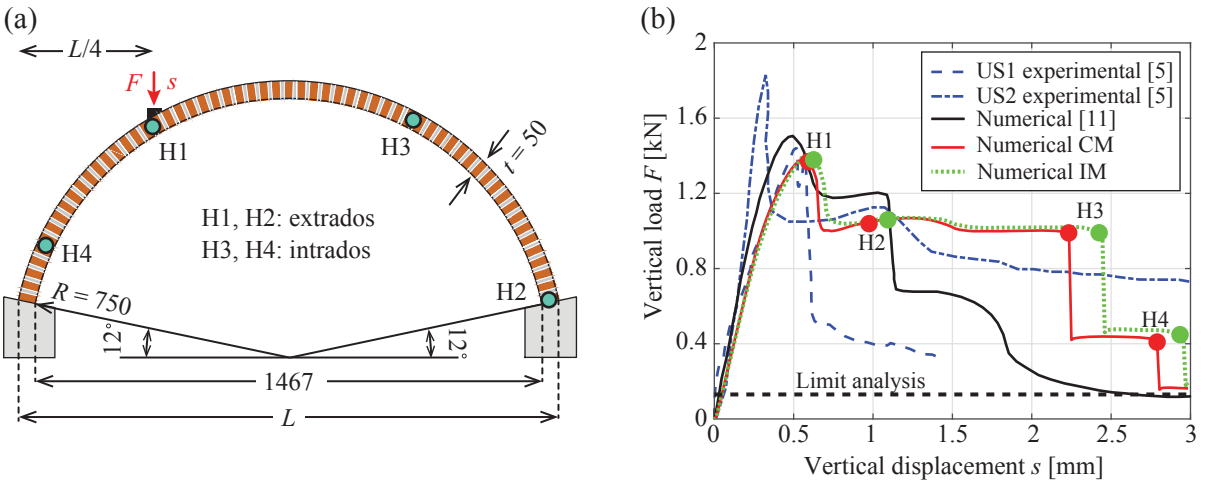

Figure 3: Unreinforced arches tested by Oliveira [5]: (a) geometry (dimensions in mm), loading conditions and experimental hinge (H) location, (b) experimental and numerical load-displacement global curves.

all solutions in terms of initial stiffness, collapse load and ductility. The curves referring to the CM and IM show slight discrepancies caused by the intrinsic differences between the two modeling assumptions. For instance, the mechanical characteristics assigned to each interface FEs are derived assuming, in a simplified manner, a constant mortar thickness of $10\,\mathrm{mm}$, thus failing to describe the small variation of thickness characterizing each mortar joint starting from the intrados to the extrados of the arch. Moreover, unlike IM, CM adopts a nonlocal integral formulation which consistently affects the evolution of degrading mechanisms.

Moreover, in Figure 3(b), the collapse load value evaluated by the classical limit analysis is depicted with dashed black line. This is estimated following the three hypotheses of Heyman [6]: masonry has no tensile strength, masonry has infinite compressive strength and sliding cannot occur between joints. It is noted that both numerical and experimental response curves approach the limit value from above, thus predicting a higher peak load. This interesting aspect is caused by the not negligible tensile strength of the mortar, which moves away from the first Heyman's hypothesis, as more in detail investigated in [8, 15].

As for the failure mechanism, this experimentally involves the formation of the classical four flexural hinges located at the intrados and extrados, alternatively (Figure 3(a)). Same results are obtained with the proposed numerical models, as evident from Figure 4(a) and (b) which contain the arch deformed configurations at the end of the analyses for IM and CM, respectively. The distribution of the damage variable D defined in Eq. (4) is also illustrated in Figure 4(b), showing that damage variable, varying between 0 and 1 according to its physical meaning, is concentrated in the zones where tensile stresses are expected to be higher. The onset of fully

cracked sections, corresponding to the formation of nonlinear hinges, is the cause of the steep load drops characterizing the load-displacement global curve in Figure 3(b), as indicated by the green and red circle markers. Finally, it should be emphasized that the two models provide indistinguishable results in terms of deformed structural configuration and predict location and order of formation of the hinges in accordance with the experimental outcomes.

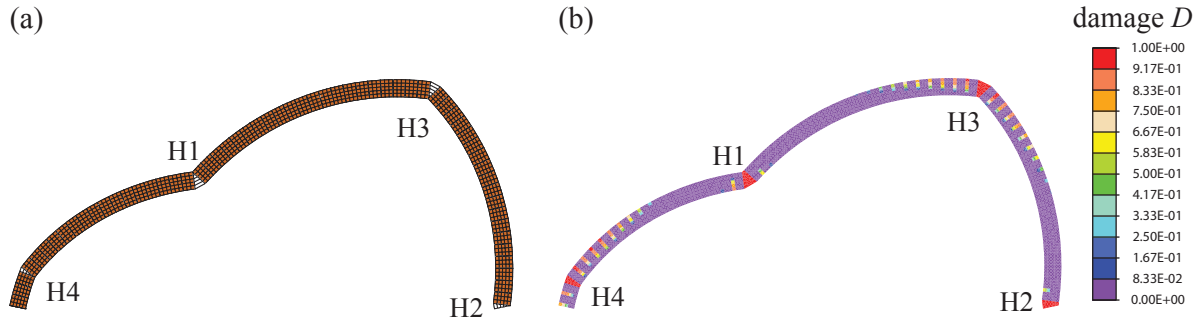

Figure 4: Numerical failure mode of the unreinforced arches tested by Oliveira [5]: (a) deformed shape obtained with IM, (b) deformed shape and distribution of the damage variable D obtained with CM.

3.2 Response of GFRM strengthened arches

The response of the GFRP strengthened arches is analyzed by employing the CM. As mentioned before, three main strengthening approaches were tested in [5]. Here, continuous configuration at the extrados is considered and numerically reproduced. The experimental set was composed of two arches (CSE1 and CSE2) strengthened with two continuous GFRP strips of $50\,\mathrm{mm}$ width, and the other two arches (CSE3 and CSE4) with two GFRP strips $80\,\mathrm{mm}$ width each. In Figure 5(a), the strengthening arrangement applied over the external substrate is schematically shown.

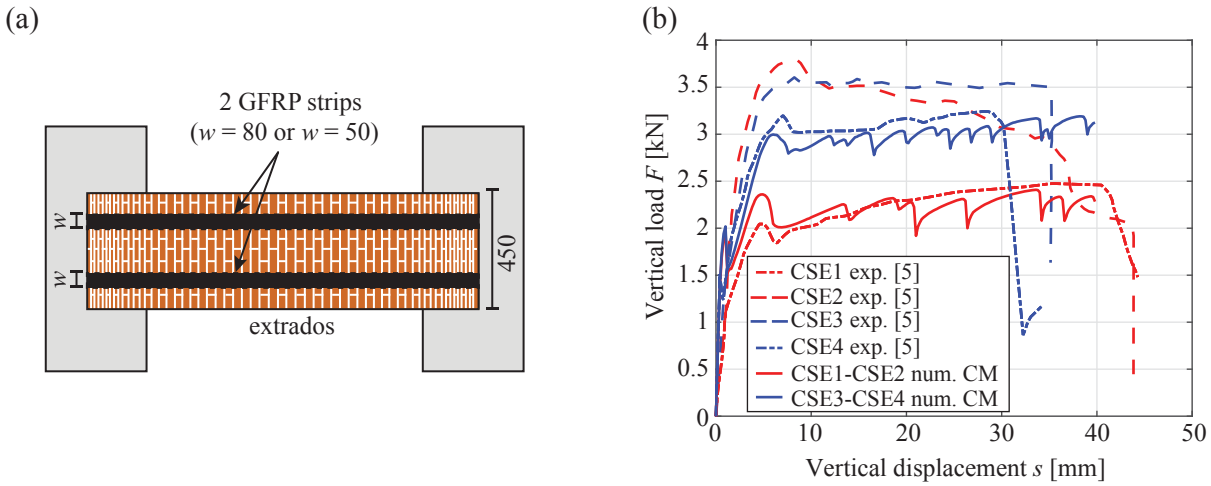

Figure 5: Strengthened arches tested by Oliveira [5]: (a) location of continuous extrados strengthening (dimension in mm), (b) experimental and numerical load-displacement global curves.

Two numerical models are considered to reproduce the different configurations by varying the size of the strips for the reinforcement and assuming the geometrical characteristic provided

in [22]. Young's modulus is set equal to $E^r = 80000\,\mathrm{MPa}$, according to the experimental results of the tensile tests performed on several GFRP samples [22]. The reduced stiffness, characterizing the second branch of the bilinear stress-strain relationship in tension, is assumed equal to $H^r = 0.01E^r$. The tensile strength, $\sigma_0^r = 200\,\mathrm{MPa}$, is calibrated to reproduce the experimental response and this is representative of both the reinforcement tensile strength and the reinforcement/masonry interaction behavior.
Figure 5(b) shows the comparison of the vertical load-vertical displacement global curves numerically and experimentally evaluated. Results referring to the configuration with $50\,\mathrm{mm}$ GFRP strips are depicted in red color, whereas those related to $80\,\mathrm{mm}$ GFRP strips are reported in blue color. Overall, a good agreement emerges between the experimental and numerical responses. The sliding failure characterized all the experimental specimens CSE, almost certainly due to their weak resistance against shear mode. The failure mechanism exhibited during testing is illustrated in Figure 6(a). It involves the formation of three hinges: in particular, a sliding hinge was located close to the right support. In Figure 6(b) the deformed numerical configuration is shown referring to the end of the analysis and to the case of strips $50\,\mathrm{mm}$ wide. According to the experimental outcomes, two sliding hinges appear. The first is located underneath the loading point, the second close to the right support. The numerical failure mechanism and the damage distribution shown in Figure 6(b) are representative of both the strengthening configurations. In fact, it is noted that the increase of the GFRP strips size from $50\,\mathrm{mm}$ to $80\,\mathrm{mm}$ did not produce significant variations in the structural response in terms of failure mechanism. Although this type of strengthening does not permit joint opening at the extrados, a widespread damage distribution seems to appear in the numerical model at the location opposite to the load application.

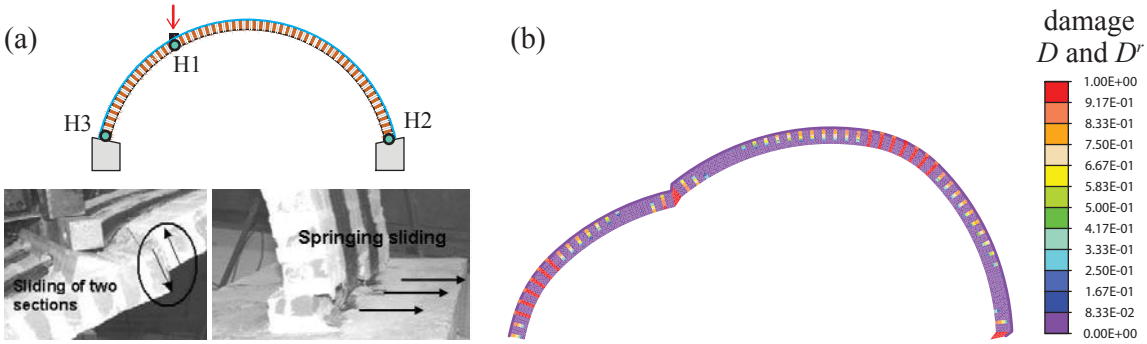

Figure 6: Externally strengthened masonry arches tested by Oliveira [5]: (a) experimental failure mechanism [5, 22], (b) numerical failure mechanism and distribution of the damage variables D and D^r obtained with CM.

4 CONCLUSIONS

- This paper presented two micromechanical FE models for the analysis of the in-plane response of masonry arches. These are based on the same constitutive assumptions, but adopt different strategies to model mortar joints. The CM considers the mortar as a continuous material modeled with 4-node isoparametric FEs, whereas the IM discretizes each mortar joint by means of 2+2 zero thickness interface elements. Linear elastic behavior is assumed for bricks, whereas a coupled damage-friction constitutive law is adopted for mortar to account for flexural and shear failure mechanisms.

- Effectiveness of the models in describing maximum strength and collapse modes of unreinforced and strengthened arches was proved by comparison with experimental outcomes.
- Satisfactory agreement is found between numerical and experimental results as regards the unreinforced case. The numerical load-displacement global curves, as well as the four hinge mechanism, well match the experimental counterpart. Moreover, the two numerical models provided very similar structural responses with only slight discrepancies caused by the different modeling assumptions. Hence, it emerged that the adoption of interface elements to model response of mortar joints is an efficient alternative to the use of continuum finite elements.
- The numerical results referring to strengthened arches with GFRP strips bonded at the extrados are encouraging. Despite the reinforcement was modeled in a simplified way by means of truss elements with mechanical properties representative of both reinforcement itself and its interaction behavior with the substrate, the change of the structural response with respect to the unreinforced case is well reproduced. The presence of the reinforcement prevented the hinge mechanism formation and let the shear sliding mechanism to prevail.
- Further improvements of the model could be performed by introducing the explicit modeling of the reinforcement-substrate interaction in order to distinguish failure mechanisms due to debonding and reinforcement rupture. To this end proper interface elements connecting masonry and reinforcement [23, 24] could be considered. Moreover, the constitutive assumptions could be modified and enriched to account for the nonlinear mechanisms involving the bricks, as masonry crushing is likely to occur in strengthened arches due to the onset of high compressive stresses.

REFERENCES

[1] P. Zampieri, N. Simoncello, C.D. Tetougueni, C. Pellegrino, A review of methods for strengthening of masonry arches with composite materials. *Engineering Structures*, **171**, 154–169, 2018.

[2] V. Alecci, F. Focacci, L. Rovero, G. Stipo, M. De Stefano, Intrados strengthening of brick masonry arches with different FRCM composites: Experimental and analytical investigations. *Composite Structures*, **176**, 898–909, 2017.

[3] F.G. Carozzi, C. Poggi, E. Bertolesi, G. Milani, Ancient masonry arches and vaults strengthened with TRM, SRG and FRP composites: Experimental evaluation. *Composite Structures*, **187**, 466–480, 2018.

[4] A. Borri, P. Casadei, G. Castori, J. Hammond, Strengthening of brick masonry arches with externally bonded steel reinforced composites. *Journal of Composites for Construction*, **13(6)**, 468–475, 2009.

[5] D.V. Oliveira, I. Basilio, P.B Lourenço, Experimental behavior of FRP strengthened masonry arches. *Journal of Composites for Construction*, **14**, 312–322, 2010.

[6] J. Heyman, The stone skeleton. *International Journal of Solids and Structures*, **2**, 249–279, 1966.

[7] C. Casapulla, L. Cascini, F. Portioli, R. Landolfo, 3D macro and micro-block models for limit analysis of out-of-plane loaded masonry walls with non-associative Coulomb friction. *Meccanica*, **49(7)**, 1653–1678, 2014.

[8] E. Bertolesi, G. Milani, F.G. Carozzi, C. Poggi, Ancient masonry arches and vaults strengthened with TRM, SRG and FRP composites: Numerical analyses. *Composite Structures*, **187**, 385–402, 2018.

[9] M. Pepe, M. Pingaro, P. Trovalusci, Limit Analysis approach for the in-plane collapse of masonry arches. *Proceedings of the Institution of Civil Engineers-Engineering and Computational Mechanics*, 1-43, 2021.

[10] E. Bertolesi, G. Milani, R. Fedele, Fast and reliable non-linear heterogeneous FE approach for the analysis of FRP-reinforced masonry arches. *Composites Part B: Engineering*, **88**, 189–200, 2016.

[11] P. Di Re, D. Addessi, E. Sacco, A multiscale force-based curved beam element for masonry arches. *Computers & Structures*, **208**, 17–31, 2018.

[12] C. Gatta, D. Addessi, F. Vestroni, Static and dynamic nonlinear response of masonry walls. *International Journal of Solids and Structures*, **155**, 291–303, 2018.

[13] E. Sacco, D. Addessi, K. Sab, New trends in mechanics of masonry. *Meccanica*, **53(7)**, 1565–1569, 2018.

[14] A.M. D'Altri, V. Sarhosis, G. Milani, J. Rots, S. Cattari, S. Lagomarsino, E. Sacco, A. Tralli, G. Castellazzi, S. de Miranda, Modeling strategies for the computational analysis of unreinforced masonry structures: review and classification. *Archives of Computational Methods in Engineering*, 1–33, 2019.

[15] M. Nocera, C. Gatta, D. Addessi, D. Liberatore, Micromechanical modeling of unreinforced masonry arches accounting for flexural hinges and shear slidings. *Accepted for publication*.

[16] E. Sacco, A nonlinear homogenization procedure for periodic masonry. *European Journal of Mechanics-A/Solids*, **28**, 209–222, 2009.

[17] D. Addessi, C. Gatta , S. Marfia, E. Sacco, Multiscale analysis of in-plane masonry walls accounting for degradation and frictional effects. *International Journal for Multiscale Computational Engineering*, **18(2)**, 159–180, 2020.

[18] D. Addessi, P. Di Re, C. Gatta , E. Sacco, Multiscale analysis of out-of-plane masonry elements using different structural models at macro and microscale. *Computers & Structures*, **247**, 106477, 2021.

[19] F. Gobbin, G. de Felice, J. Lemos, A Discrete Element Model for Masonry Vaults Strengthened with Externally Bonded Reinforcement. *International Journal of Architectural Heritage*, 1–14, 2020.

[20] D. Addessi, E. Sacco, P. Di Re, Multi-scale analysis of masonry structures. *Proceedings of the International Masonry Society Conferences*, **0(222279)**, 307–323, 2018.

[21] C. Carloni, D.A. Bournas, F.G. Carozzi et al., Fiber reinforced composites with cementitious (inorganic) matrix. *Design procedures for the use of composites in strengthening of reinforced concrete structures*, Springer, Dordrecht, 349–392, 2016.

[22] I. Basilio, Strengthening of arched masonry structures with composite materials, 2007.

[23] B. Pantò, F. Cannizzaro, S. Caddemi, I. Caliò, C. Chácara, P.B. Lourenço, Nonlinear modelling of curved masonry structures after seismic retrofit through FRP reinforcing. *Buildings*, **7(3)**, 2017.

[24] C. D'Ambra, G.P. Lignola, A. Prota, F. Fabbrocino, E. Sacco, FRCM strengthening of clay brick walls for out of plane loads. *Composites Part B: Engineering*, **174**, 107050, 2019.